

# Effect of the proximity to the $0^\circ/90^\circ$ interface on Energy Release Rate of fiber/matrix interface crack growth in the $90^\circ$ -ply of a cross-ply laminate under tensile loading

Luca Di Stasio<sup>a,b</sup>, Janis Varna<sup>a</sup>, Zoubir Ayadi<sup>b</sup>

<sup>a</sup>Luleå University of Technology, University Campus, SE-97187 Luleå, Sweden

<sup>b</sup>Université de Lorraine, EEIGM, IJL, 6 Rue Bastien Lepage, F-54010 Nancy, France

---

## Abstract

Models of Representative Volume Elements (RVEs) of cross-ply laminates with different geometric configurations and damage states are studied. Debond growth is characterized by the estimation of the Mode I and Mode II Energy Release Rate (ERR) using the Virtual Crack Closure Technique (VCCT). It is found that the presence of the  $0^\circ/90^\circ$  interface and the thickness of the  $0^\circ$  layer have no effect, apart from laminates with *ultra-thin*  $90^\circ$  plies where it is however modest. The present analysis support the claim that debond growth is not affected by the ply-thickness effect.

**Keywords:** Polymer-matrix Composites (PMCs), Fibre/matrix bond, Debonding, Finite Element Analysis (FEA)

---

## 1. Introduction

Since the development of the *spread tow* technology or “FUKUI method” [1], significant efforts have been directed toward the characterization of *thin-ply* laminates [2, 3, 4, 5, 6, 7, 8, 9, 10, 11] and their application to mission-critical structures in the aerospace sector [12].

At the lamina level, the use of *thin-ply*s leads to more regular and homogeneous microstructures [6, 9]. Measurements of ply level properties (tensile and compressive modulus, Poisson’s ratio, ultimate tensile strength, tensile onset of

damage, interlaminar shear strength) on Uni-Directional (UD) specimens ( $[0_m^\circ]$   
10 and  $[90_m^\circ]$ ) revealed no remarkable difference with average properties available in  
the literature for the same type of fiber, nor showed any particular dependence  
on the ply thickness [9]. Only an increase of the ultimate compressive strength  
in the fiber direction was observed with very thin plies ( $\sim 4$  fiber diameters),  
although with very scattered values. The authors claim the increase to be due  
15 to the fiber arrangement's increased regularity which prevents the onset of fiber  
microbuckling [9]. A number of researchers [2, 3, 4] has reported improvements  
in fatigue life with the use of *thin-ply*s, which are explained as a consequence of  
delayed propagation of free edge delaminations and intralaminar cracks. Several  
researchers have analyzed the effect of *thin-ply*s on damage development under  
20 static [3, 4, 5, 6, 7, 8, 9], fatigue [2, 3, 4, 5, 9] and impact loadings [3, 4, 5, 9]. It  
seems apparent that *thin-ply* laminates possess an increased ability to delay, and  
in some cases even suppress, the onset and propagation of intralaminar cracks  
(called often transverse or matrix or micro-cracks).

The first stage in the appearance of transverse cracks is known to be the occur-  
25 rence of fiber/matrix interface cracks (also referred to as debonds), which grow  
along the fiber arc direction, then kink out of the interface and coalesce forming  
a transverse crack [13]. Different approaches have been applied to model the  
initiation and growth of debonds [14]. The Cohesive Zone Model (CZM) has  
been used to mimic the propagation of debonds along fiber interfaces; coupled  
30 with a failure criterion for the matrix, it has provided simulations of the growth  
of transverse cracks starting from a virgin material [15, 16, 17, 18]. The strength  
of the CZM, and its main requirement for a correct implementation, lies in the  
elimination of the stress and displacement singularity that exists at the crack  
tip in the Linear Elastic Fracture Mechanics (LEFM) solution, as the crack tip  
35 is not explicitly modeled and the failure process is "smeared" over the finite  
length of the cohesive element. The main advantages of this approach are the  
possibility to observe the development of a simulated crack path and to record  
a load-displacement curve to be compared with experimental measurements.  
The fracture toughness (or critical Energy Release Rate) dependence on mode-

40 mixity in the case of the interface crack [19] was successfully incorporated in  
 a cohesive zone model by Freed and Banks-Sills [20]. However, different prob-  
 lems were reported [21] on the use of cohesive elements to simulate a bimaterial  
 interface crack. It was observed that, for mixed-mode fracture in general, a sin-  
 gle cohesive zone length might not simultaneously cancel both the tensile and  
 45 shear stress singularity at the crack tip and thus fail to satisfy the fundamental  
 requirement of the CZM approach. Also, it was concluded that energy dissipa-  
 tion at the cohesive zone tip could be neglected only with high enough values  
 of the initial tensile and shear stiffnesses. A further issue which arises in the  
 use of cohesive elements is the selection of appropriate values for the material  
 50 parameters required by the model (critical stress and Energy Release Rate).  
 Two options are available: adopting values measured from macroscopic tests  
 (e.g. Double Cantilever Beam) or calibrating the parameters through inverse  
 estimation by approximation of the macroscopic stress-strain response of the  
 specific specimen the RVE modeled is representing. Finally, the failure mech-  
 55 anisms proposed by the Cohesive Zone Model might not represent the actual  
 physics of the fiber/matrix interface failure process. It was shown [22] that the  
 triaxiality of the matrix stress state in the inter-fiber region may be the driver  
 of brittle matrix failure at or very close to the interface through a cavitation-like  
 mechanism [23]. It thus seems likely that brittle failure at the interface may cre-  
 60 ate an initial flaw from which debonding occurs in a fast and unstable manner,  
 that could be modeled by the classic Griffith's criterion of LEFM. Linear Elastic  
 Fracture Mechanics obviates many of the drawbacks highlighted for Cohesive  
 Zone Modeling. The analysis focuses on the evaluation of Mode I and Mode  
 II Energy Release Rate (ERR) at the crack tip by means of the Virtual Crack  
 65 Closure Technique (VCCT) [24] or the J-Integral method [25]. The stress and  
 strain fields, required for the ERR computation, can be solved by application of  
 different methodologies such as analytical solutions [26], the Boundary Element  
 Method (BEM) [27] or the Finite Element Method (FEM) [28]. This approach  
 presents nonetheless some limitations: it describes propagation of the debond  
 70 and not its initiation; the role of friction in the contact zone is still an open

issue; consensus is still lacking on a proper criterion for crack propagation in mixed mode. Finite fracture mechanics [29] is one way to address the initiation problem. Different studies have followed the LEFM approach and analyzed models of one or two fibers in an effectively infinite matrix [30, 31, 32, 33, 34] and of an hexagonal cluster of fibers in an effectively infinite homogenized UD composite [35, 28]. The problem of debond growth along the fiber-matrix interface in a cross-ply laminate has been only treated very recently in [36, 37], where authors embed a single partially debonded fiber in an effectively infinite homogenized  $90^\circ$  ply bounded by homogenized  $0^\circ$  layers. Thus, the effect of debond-debond interaction and of the relative proximity of a  $0^\circ/90^\circ$  interface on debond ERR in cross-ply laminates is yet to be addressed. The present work is devoted to this problem. Our interest however is not to investigate the sequence of failure events, which would require knowledge of appropriate failure criteria and properties, but rather to understand which parameters may make debond growth energetically favorable and which may prevent it. Models of Repeating Unit Cells (RUCs) are developed to represent laminates with different degrees of damage in the  $90^\circ$  ply (here only in the form of debonds). The number of fully bonded fibers across the thickness of the  $90^\circ$  ply is varied in order to investigate the effect of the proximity of the  $0^\circ/90^\circ$  interface. The thickness of the bounding  $0^\circ$  layers is also used as a parameter of the study. The stress and strain fields are solved with the Finite Element Method in Abaqus [38] and the debond (crack) is characterized by its Mode I and Mode II ERR calculated with the VCCT.

## 2. RVE models & FE discretization

### 2.1. Introduction & nomenclature

In the present work, we investigate debond development under in-plane longitudinal tension in  $[0_{m \cdot k \cdot 2L}^\circ, 90_{k \cdot 2L}^\circ, 0_{m \cdot k \cdot 2L}^\circ]$  laminates. The interaction between debonds in the presence of an interface with a stiff layer is studied with the use of different Repeating Unit Cells (RUCs) (see Figures 1 and 2 in Sec. 2.2), in

100 which only the central fiber is partially debonded. Repetition of the composite RUC occurs along the in-plane laminate  $0^\circ$ -direction (corresponding to specimen axial direction and RUC horizontal direction in Figures 1 and 2), thus representing a cross-ply laminate with a thin or even ultra-thin  $90^\circ$  ply in the middle.

105 All the RUCs present regular microstructures with fibers placed according to a square-packing configuration characterized by the repetition of the same one-fiber unit cell of size  $2L \times 2L$ , where  $L$  is a function of the fiber volume fraction  $V_f$  and the fiber radius according to

$$L = \frac{R_f}{2} \sqrt{\frac{\pi}{V_f}}. \quad (1)$$

The choice of a square-packing configuration with a controlled number of  
 110 fibers is motivated by the fact that our objective is to determine the effect of different geometrical and mechanical factors on debond Energy Release Rate, such as fiber volume fraction, the presence of undamaged and partially debonded fibers, the presence of the  $0^\circ/90^\circ$  interface. The use of a regular microstructure allows us to isolate and identify the different contributions, which would be  
 115 otherwise “smeared out” with the use of randomized distribution with a large number of fibers. Each fiber in the model has the same radius  $R_f$ , equal to  $1 \mu m$ . This specific value has no physical meaning per se and it has been selected for simplicity. It is useful to observe that, in a linear elastic solution subject to non-holonomic constraints as the one described in the present article, the ERR is  
 120 proportional to the geometrical dimensions of the model and thus re-evaluation of the ERR for fibers of any size requires just a multiplication. Furthermore, it is worth to point out that  $V_f$  is the same in the one-fiber unit and in the overall RUC, i.e. no clustering of fibers is considered.

The thickness of the  $90^\circ$  ply depends on the number  $k$  of fiber rows present  
 125 across the thickness (the vertical or  $z$  direction in Figures 1 and 2) according to

$$t_{90^\circ} = k \cdot 2L. \quad (2)$$

On the other hand, the thickness of  $0^\circ$  layers can be assigned freely as a multiple of the  $90^\circ$  ply thickness as

$$t_{0^\circ} = m \cdot t_{90^\circ} \quad (3)$$

where  $m$  is an arbitrary integer. Thus, the thickness ratio  $m$  represents one additional parameter for the investigation.

130 In the following, let us consider in-plane coordinates  $x$  and  $y$ , and assume that the laminate  $0^\circ$ -direction is aligned with the  $x$ -axis. In the presence of a load in the  $x$ -direction, the strain in the  $y$ -direction is small, due to the very small Poisson's ratio of the laminate. Debonds are present only in the  $90^\circ$  layer and are considered to be significantly longer in the fiber direction than in the arc direction [39]. Therefore we use 2D models under the assumption of plane strain, 135 defined in the  $x - z$  section of the composite. The study presented in this paper thus applies to long debonds and its focus is on understanding the mechanisms of growth along their arc direction. The laminates are assumed to be subject to tensile strain, which is applied in the form of a constant displacement in the 140  $x$ -direction along both vertical boundaries of the RUC as shown in Figure 3.

We assume damage to be present only in the central “row” of fibers of the  $90^\circ$  layer in the form of multiple debonds appearing at different regular intervals along the loading (horizontal) direction. The number of fibers  $n$  present in the horizontal direction of the RUC (Figures 1 and 2) controls the distance, 145 in terms of fully bonded fibers, between consecutive debonds: if the RUC has  $n$  fibers in the horizontal direction, two consecutive debonds are separated by  $n - 1$  undamaged fibers. The RUCs considered are thus Representative Volume Elements (RVEs) of cross-ply laminates with a certain distribution of debonds in the middle  $90^\circ$  layer.

150 In summary, the models are differentiated by: first, the spacing between debonds along the horizontal direction in the  $90^\circ$  layer, which corresponds to the number  $n$  of fibers in the RUC's horizontal direction; second, the thickness of the middle  $90^\circ$  ply measured in terms of the number  $k$  of fiber rows in the vertical direction;

third, the factor  $m$  which provides the thickness of  $0^\circ$  layers as a multiple of  
155 the  $90^\circ$  ply thickness. It thus seems natural to introduce a common notation  
for the RUCs as  $n \times k - m \cdot t_{90^\circ}$ .

An additional family of RUCs is considered, in which: only one partially debonded  
fiber is present; the  $0^\circ$  layer is absent; different combinations of displacement  
boundary conditions are applied to the upper surface. The application of cou-  
160 pling of horizontal displacements  $u_x$  along the right and left sides allows for  
repetition along the horizontal direction. When the upper boundary of the  
RUC is left free, we define the  $1 \times 1 - free$  model. If coupling of the vertical  
displacements  $u_z$  is applied to the upper boundary (coupling condition), we de-  
fine instead the  $1 \times 1 - coupling$  model. In the case a linear distribution of the  
165 horizontal displacement  $u_x$  is applied to the upper boundary (H-condition), the  
model is referred to as  $1 \times 1 - H$ . Finally, when the linear distribution of the hor-  
izontal displacement  $u_x$  is superimposed to the condition of coupling of the ver-  
tical displacements  $u_z$  on the upper boundary, we have the  $1 \times 1 - coupling + H$ .  
Further details about this family of RUCs and the corresponding laminate RVE  
170 can be found in [40].

## 2.2. Description of modelled Representative Volume Elements (RVEs)

The first family of Representative Volume Elements (RVEs) is represented  
in Figure 1. It represents a set of  $[0_{m \cdot 1 \cdot 2L}^\circ, 90_{1 \cdot 2L}^\circ, 0_{m \cdot 1 \cdot 2L}^\circ]$  laminates with an  
ultra-thin  $90^\circ$  layer, constituted by a single row of fibers across the thickness.  
175 Debonds appear at regular intervals measured in terms of number  $n - 1$  of fully  
bonded fibers present between them, which in turn correspond to the number  
of fibers along the horizontal direction of the RVE as highlighted in Fig. 1.  
They are thus the  $n \times 1 - m \cdot t_{90^\circ}$  models, where  $m = 1, 10$  and  $n$  is an integer  
 $\geq 1$  ( $n = 1$  corresponds to the case of a debond appearing on all the fibers in  
180 the central  $90^\circ$  layer). These models are geometrically extreme, but allow to  
focus on the interaction between debonds and the inter-ply  $0^\circ/90^\circ$  interface.  
Furthermore, the *spread tow* technology is today capable of producing cross-ply  
laminates with the central  $90^\circ$  layer thickness only 4–5 times the fiber diameter,

as shown for example in [6], which may in future give practical relevance even

185 to such extreme case.

The second set of models considers instead cross-ply laminates with a central  
90° ply of variable thickness, measured in terms of number  $k$  of fiber rows  
“stacked” in the vertical direction in Figure 2. Once again, debonds appear in  
the central row only at regular intervals measured in terms of number  $n - 1$   
190 of fully bonded fibers present between them, as highlighted in Fig. 2. These  
models are thus the  $n \times k - m \cdot t_{90^\circ}$  models, where  $m = 1, 10$ ,  $k > 1$  and  $n$   
is an integer  $\geq 1$  ( $n = 1$  corresponds to the case of a debond appearing on all  
fibers of the central fiber row in the 90° layer). By increasing the number  $n$   
of fibers in the horizontal direction in the RUC, decreasing levels of damage  
195 (debonds spaced further apart and the interaction between debonds becomes  
less important) are considered to be present in the laminate. By increasing the  
number  $k$  of fiber rows, the thickness of the 90° layer is increased and the effect  
of the relative proximity of the inter-ply 0°/90° interface can thus be studied.  
Finally, by increasing the factor  $m$ , the thickness of the 0° layers is increased for  
200 a given thickness of the 90°, which allows the investigation of the 0° ply-block  
effect [41].

### 2.3. Finite Element (FE) discretization

The RUCs are discretized and solved with the Finite Element Method (FEM)  
using the commercial FEM package Abaqus [38]. The total length and height of  
205 a RUC are determined by the number of fibers  $n$  in the horizontal direction, the  
number of fiber rows  $k$  across the thickness and the thickness ratio  $m$  (see Sec. 2.1  
and Sec. 2.2). The debond appears symmetrically with respect to the  $x$  axis (see  
Fig. 3) and we characterize it with the angular size  $\Delta\theta$  (the full debond size is  
thus  $2\Delta\theta$ ). In the case of large debond sizes ( $\geq 60^\circ - 80^\circ$ ), a region of size  $\Delta\Phi$   
210 to be determined by the solution itself appears at the crack tip. In this region,  
called the *contact zone*, the crack faces are in contact and slide on each other.  
Due to existence of the contact zone, frictionless contact is considered between  
the two crack faces to avoid interpenetration and allow free sliding. Symmetry



with respect to the  $x$  axis is applied on the lower boundary. Kinematic coupling  
215 on the  $x$ -displacement is applied along the left and right boundaries of the model  
in the form of a constant  $x$ -displacement  $\pm \bar{\varepsilon}_x nL$ , corresponding to laminate  $x$ -  
strain  $\bar{\varepsilon}_x$  equal to 1%. The bimaterial interface crack problem belongs to the  
class of *receding contact* [27, 42], i.e. such that the contact zone in the final  
configuration is smaller than in the initial one. It was shown that this class of  
220 problems has some peculiar properties [43, 44], which are valid both with and  
without friction at the interface [27, 42]: size and shape of the contact zone  
remain the same upon a change in the magnitude of the applied load; only a  
change in the disposition of the applied load causes a change in the size and  
shape of the contact zone; displacements, stresses and strains (and consequently,  
225 Energy Release Rate) are directly proportional to the value of the applied load.  
Thus, although our interest is to compare the relative magnitude of Mode I  
and Mode II ERR among different configurations, the results presented could  
be used to compute the ERR at different levels of the applied strain through a  
simple multiplication.

230 The FEM model is discretized using second order, 2D, plane strain triangular  
(CPE6) and rectangular (CPE8) elements. In the crack tip neighborhood, a  
refined regular mesh of quadrilateral elements with almost unitary aspect ratio  
is needed to ensure a correct evaluation of the ERR. The angular size  $\delta$  of an  
element in this refined region close to the crack tip is by design equal to  $0.05^\circ$ .

235 The crack faces are modeled as element-based surfaces with a frictionless small-  
sliding contact pair interaction. The Mode I, Mode II and total Energy Release  
Rates (ERRs) (respectively  $G_I$ ,  $G_{II}$  and  $G_{TOT}$ ) represent the main result of  
the numerical analysis. They are computed using the VCCT [24] implemented  
in a custom Python routine. Glass fiber and epoxy are considered throughout  
240 this article, and it is assumed that their response always lies in the linear elastic  
domain. The effective UD properties are computed using Hashin's Concentric  
Cylinder Assembly model [45] with the self-consistency scheme for the out-of-  
plane shear modulus of Christensen [46]. The properties used are listed in  
Table 1. The model was validated with respect to BEM results of [47, 33];

245 considerations about the order of accuracy can be found in [40].

### 3. Results & Discussion

#### 3.1. Effect of the proximity of the $0^\circ/90^\circ$ interface and of the thickness of the $0^\circ$ layer on debond ERR for highly interactive debonds

We first focus our attention on the model  $1 \times 1 - m \cdot t_{90^\circ}$ , which represents  
 250 a particular case of the family  $n \times 1 - m \cdot t_{90^\circ}$ . It corresponds to a cross-ply laminate in which the central  $90^\circ$  ply is constituted by only one fiber row, in which each fiber possesses a debond appearing on alternating sides. The model thus represents an extreme idealization, in the sense that: first, the central  $90^\circ$  layer is the thinniest that can be conceived, which allows us to  
 255 investigate the direct effect of the proximity of the  $0^\circ/90^\circ$  interface on debond ERR; second, a very particular damage state is present for which every fiber is partially debonded from the surrounding matrix, corresponding to the most severe damage state that can occur in the  $90^\circ$  ply when considering debonds as the only mechanism of damage. We are thus focusing on the presence of the  
 260  $0^\circ/90^\circ$  interface and on the thickness of the  $0^\circ$  layer, by considering the ratio  $m = \frac{t_{0^\circ}}{t_{90^\circ}}$  of ply thicknesses as a free parameter.

In Figures 4 and 5 it is possible to observe respectively the Mode I and Mode II ERR for models  $1 \times 1 - m \cdot t_{90^\circ}$  with  $m = 1, 10, 100$ . Mode I ERR is practically unaffected by the  $0^\circ$  layer thickness, only a marginal increase  $\leq 1\%$  can be seen  
 265 when  $m$  is increased from 1 to 10. No further observable change is present when  $m$  is increased to 100. Moreover, the contact zone onset, which corresponds to the first value of  $\Delta\theta$  such that  $G_I = 0$ , is always equal to  $70^\circ$  irrespective of the value of  $m$ . A more remarkable, albeit small, effect of the  $0^\circ$  layer thickness can be observed for Mode II when  $m$  is increased from 1 to values  $\geq 10$ . For  
 270 open cracks, i.e. when no contact zone is present and thus  $\Delta\theta$  is smaller than  $70^\circ$ , increasing the  $0^\circ$  layer thickness causes a reduction of Mode II ERR; while for closed cracks, when a contact zone is present and  $\Delta\theta > 70^\circ$ , the increase in thickness leads to an increase in ERR.

In order to understand the interaction mechanism between the  $0^\circ/90^\circ$  interface  
 275 and the debond, Mode I and Mode II ERR are reported respectively in Figures 4  
 and 5 for models  $1 \times 1 - free$ ,  $1 \times 1 - H$ ,  $1 \times 1 - coupling$  and  $1 \times 1 - coupling + H$ .  
 These RUCs all present equivalent boundary conditions and it is here useful  
 to recall their characteristics: in model  $1 \times 1 - free$  the upper boundary is  
 left free; coupling conditions on the vertical displacements  $u_z$  are applied to  
 280 the upper boundary in model  $1 \times 1 - coupling$  (coupling condition); in model  
 $1 \times 1 - H$  a linearly distributed horizontal displacement  $u_x$  is applied to the upper  
 boundary (H-condition); in model  $1 \times 1 - coupling + H$  coupling conditions on  
 the vertical displacements  $u_z$  and a linearly distributed horizontal displacement  
 $u_x$  are imposed together on the upper boundary. Given that the presence of a  
 285  $0^\circ$  layer provides two constraints: first, it tends to keep the  $90^\circ$  layer boundary  
 straight; second, it forces a more homogeneous horizontal displacement at the  
 $90^\circ$  layer boundary; the equivalent boundary conditions of  $1 \times 1 - coupling$ ,  
 $1 \times 1 - H$  and  $1 \times 1 - coupling + H$  represent an extreme case respectively of  
 the first constraint ( $1 \times 1 - coupling$ ), the second constraint ( $1 \times 1 - H$ ) and the  
 290 two together ( $1 \times 1 - coupling + H$ ). The case  $1 \times 1 - free$  constitutes instead  
 the base case (absence of  $0^\circ$  layer), on which comparisons are built.

Observing Figure 4, it is possible to notice that the values of  $G_I$  for the  $1 \times$   
 $1 - free$  and the  $1 \times 1 - coupling$  models represent respectively a lower and  
 an upper bound for the  $1 \times 1 - m \cdot t_{90^\circ}$  RVEs: this is true with respect to  
 295 the value of  $G_I$  as well as of contact zone onset ( $60^\circ$  for  $1 \times 1 - free$ ,  $70^\circ$  for  
 $1 \times 1 - m \cdot t_{90^\circ}$ ,  $80^\circ$  for  $1 \times 1 - coupling$ ). When the H-condition is added to  
 the  $1 \times 1 - free$  and the  $1 \times 1 - coupling$  models, thus obtaining the  $1 \times 1 - H$   
 and  $1 \times 1 - coupling + H$  models,  $G_I$  decreases while the value of  $\Delta\theta$  at contact  
 zone onset remains unchanged ( $60^\circ$  for  $1 \times 1 - free$  and  $1 \times 1 - H$ ,  $80^\circ$  for  
 300  $1 \times 1 - coupling$  and  $1 \times 1 - coupling + H$ ). Moreover, it is possible to observe  
 that the values of  $G_I$  of  $1 \times 1 - coupling + H$  are much closer to but always greater  
 than those of  $1 \times 1 - m \cdot t_{90^\circ}$  RVEs, thus constituting a more representative upper  
 bound for the latter.

Analogous considerations are drawn with regard to Mode II (see Fig. 5). For

305 small debonds,  $\Delta\theta \leq 30^\circ$ , no significant difference in  $G_{II}$  can be seen between  
 $1 \times 1 - free$  and  $1 \times 1 - H$  and between  $1 \times 1 - coupling$  and  $1 \times 1 - coupling + H$   
in this region. With respect to  $1 \times 1 - m \cdot t_{90^\circ}$  RVEs, the first pair ( $1 \times 1 - free$   
and  $1 \times 1 - H$ ) represents the lower bound while the second pair ( $1 \times 1 - coupling$   
and  $1 \times 1 - coupling + H$ ) the upper bound. For  $30^\circ < \Delta\theta \leq 60^\circ$ ,  $1 \times 1 - H$  and  
310  $1 \times 1 - coupling + H$  provide significantly lower values of  $G_{II}$  than respectively  
 $1 \times 1 - free$  and  $1 \times 1 - coupling$ .  $G_{II}$  values of  $1 \times 1 - H$  are very close to  
 $1 \times 1 - 1 \cdot t_{90^\circ}$ , even coincident for  $\Delta\theta = 60^\circ$ . On the other hand,  $G_{II}$  values of  
 $1 \times 1 - coupling$  are very close to  $1 \times 1 - m \cdot t_{90^\circ}$  with  $m \geq 10$  and even coincident  
for  $\Delta\theta = 50^\circ$ . For  $60^\circ < \Delta\theta \leq 110^\circ$ , the situation changes.  $1 \times 1 - free$  and  
315  $1 \times 1 - coupling$  provides values of  $G_{II}$  close to each other, even coincident for  
 $\Delta\theta = 70^\circ$ . Values of  $G_{II}$  of  $1 \times 1 - H$  and  $1 \times 1 - coupling + H$  are significantly  
larger than both  $1 \times 1 - free$  and  $1 \times 1 - coupling$ . Furthermore,  $G_{II}$  values of  
 $1 \times 1 - H$  coincide with those of  $1 \times 1 - m \cdot t_{90^\circ}$  with  $m \geq 10$ . Mode II ERR of  
 $1 \times 1 - 1 \cdot t_{90^\circ}$  is instead close, but not coincident, to that of  $1 \times 1 - coupling$ .  
320 For  $\Delta\theta > 110^\circ$ ,  $G_{II}$  is the same for all models and reaches 0 at a debond size  
of around  $130^\circ$ .

These results help to understand the effect of the  $0^\circ/90^\circ$  interface on debond  
ERR. Two constraining mechanisms are present in the case of  $0^\circ/90^\circ$  interface  
that are absent in the free surface case: first, the boundary of the  $90^\circ$  layer  
325 remains straighter (effect modelled by the coupling condition in  $1 \times 1 - coupling$ );  
second, the  $x$ -strain on the  $90^\circ$  layer boundary is more uniform (effect modelled  
by the H-condition in  $1 \times 1 - H$ ).

For small debonds ( $\Delta\theta < 60^\circ - 70^\circ$ ), the presence of the  $0^\circ/90^\circ$  interface causes  
an increase of  $G_I$  and a decrease of  $G_{II}$  with respect to the free surface case.  
330 For Mode I, the fact that the  $90^\circ$  layer boundary remains straight (coupling  
condition) forces the debond to open more than in the free case, thus increasing  
 $G_I$ . However, the uniformity of the  $x$ -strain on the  $90^\circ$  layer boundary reduces  
the local (in the debond neighborhood)  $x$ -strain magnification and contains the  
increase in  $G_I$ . This corresponds in Figure 4 to the fact that Mode I ERR for  
335  $1 \times 1 - m \cdot t_{90^\circ}$  is always higher than  $1 \times 1 - free$  but lower than  $1 \times 1 - coupling$ ,

and it is best approximated by  $1 \times 1 - \text{coupling} + H$ . For Mode II in the case of small debonds, the presence of the  $0^\circ$  layer keeps the  $0^\circ/90^\circ$  interface straighter and reduces the vertical contraction of the matrix, which contributes for the most part to Mode II in this range, thus leading to a decrease of  $G_{II}$ . The small  
 340 effect of  $0^\circ$  layer thickness on Mode II (Fig. 5) can be explained in terms of local bending stiffness: a thinner  $0^\circ$  layer ( $\frac{t_{0^\circ}}{t_{90^\circ}} = 1$ ) does not keep the  $90^\circ$  layer boundary as straight as thicker  $0^\circ$  layers ( $\frac{t_{0^\circ}}{t_{90^\circ}} \geq 10$ ). In the case  $\frac{t_{0^\circ}}{t_{90^\circ}} = 1$ , the  $90^\circ$  layer boundary deforms in a way that is similar to the free surface case, but smaller in magnitude. This corresponds to the fact that for  $\Delta\theta < 60^\circ - 70^\circ$ , in  
 345 Figure 5:  $1 \times 1 - 1 \cdot t_{90^\circ}$  is best approximated by  $1 \times 1 - H$  (curved  $90^\circ$  layer boundary but uniform  $x$ -strain at the  $90^\circ$  layer boundary that disfavors  $G_{II}$ ),  $1 \times 1 - m \cdot t_{90^\circ}$ ,  $m \geq 10$  is best approximated by  $1 \times 1 - \text{coupling}$  (straight  $90^\circ$  layer boundary).

For debonds larger than  $70^\circ$ , the presence of the  $0^\circ/90^\circ$  interface causes an  
 350 increase of  $G_{II}$  with respect to the free surface case. The uniform  $x$ -strain distribution on the  $90^\circ$  layer boundary determined by the presence of the  $0^\circ$  layer causes, with respect to the free case, the matrix  $x$ -strain to be higher in the  $x \sim 0$  neighborhood and lower around  $x \sim \pm L$ , in order to keep the average  $\varepsilon_x$  at 1%. Given that for large debonds Mode II ERR is determined mostly by  
 355 the magnitude of the  $x$ -strain gap (between the matrix  $x$ -strain and the fiber  $x$ -strain), an increase of  $G_{II}$  is thus observed in the presence of the  $0^\circ/90^\circ$  interface. Again, the observed effect of the  $0^\circ$  layer thickness on Mode II for  $\Delta\theta > 60^\circ - 70^\circ$  (Fig. 5) can be discussed in terms of local  $0^\circ$  layer bending stiffness. In the free case, it is the curvature of the material around the fiber  
 360 that causes the  $x$ -strain reduction and thus a lower  $G_{II}$ . Thicker  $0^\circ$  layers ( $\frac{t_{0^\circ}}{t_{90^\circ}} \geq 10$ ) prevent this  $90^\circ$  boundary deformation to a greater extent than the thinner  $t_{0^\circ} = t_{90^\circ}$  case: the  $x$ -strain (and thus  $G_{II}$ ) increase is greater for  $\frac{t_{0^\circ}}{t_{90^\circ}} \geq 10$  than  $\frac{t_{0^\circ}}{t_{90^\circ}} = 1$ .

### 3.2. Effect of the proximity of the $0^\circ/90^\circ$ interface and of the thickness of the

$0^\circ$  layer on non-interactive debonds in a one-fiber row  $90^\circ$  ply

We turn now our attention to models  $n \times 1 - m \cdot t_{90^\circ}$ , which correspond to a cross-ply laminate in which the central  $90^\circ$  ply is constituted by only one fiber row where multiple partially debonded fibers are present with  $n - 1$  fully bonded fibers between them and debonds appear on alternating sides of consecutive damaged fibers (see Figure 1). As observed in a previous work [40], the presence of fully bonded fibers between partially debonded ones in the loading direction has a strong effect on debond ERR and controls the interaction between debonds. When  $n$  is increased, both Mode I and Mode II increase: the addition of stiffer elements, in the form of fully bonded fibers, increase the strain applied to the damaged unit and thus causes higher values of ERR. Looked from this perspective, i.e. moving from the most to the least severe state of damage, this effect is referred to as “strain magnification” [40]. There seems to exist a characteristic distance, measured in terms of fully bonded fibers, above which a change in the number of undamaged fibers affects only marginally, or even not at all, debond ERR. This distance, generally  $n \sim 20$ , marks the transition between a non-interactive solution ( $n > 20$ ) and an interactive one ( $n < 20$ ). The “strain magnification” effect thus represents the transition from the interactive to the non-interactive solution. If in Sec. 3.1 we studied the effect of the proximity of the  $0^\circ/90^\circ$  interface and of the thickness of the  $0^\circ$  layer on interactive debonds ( $1 \times 1 - \dots$ ), we analyze in the present section the effect of the  $0^\circ/90^\circ$  interface and of the  $0^\circ$  layer thickness on non-interactive ones ( $n \times 1 - \dots$  with  $n > 20$ ). Comparing Fig. 6 with Fig. 4 and Fig. 7 with Fig. 5, it is possible to observe how, as previously described, increasing the number of fully bonded fibers between consecutive debonds in the loading direction leads to an increase in Mode I and Mode II ERR. The peak  $G_I$  increases from  $1.93 \left[ \frac{J}{m^2} \right]$  in  $1 \times 1 - 1 \cdot t_{90^\circ}$  to  $3.42 \left[ \frac{J}{m^2} \right]$  in  $21 \times 1 - 1 \cdot t_{90^\circ}$ , while the peak  $G_{II}$  from  $0.86 \left[ \frac{J}{m^2} \right]$  to  $3.04 \left[ \frac{J}{m^2} \right]$ . The value of  $\Delta\theta$  at contact zone onset remains however the same ( $70^\circ$ ). The effect of the  $0^\circ$  layer thickness is instead non-existent: values of both  $G_I$  and  $G_{II}$  are coincident for  $21 \times 1 - 1 \cdot t_{90^\circ}$  and  $21 \times 1 - 10 \cdot t_{90^\circ}$ .

395 In agreement with the introductory considerations of this section and the re-  
 sults in [40], it is possible to observe in Figures 6 and 7 that  $21 \times 1 - free$  and  
 $21 \times 1 - coupling$  (in which the horizontal displacement  $u_x$  is left unconstrained on  
 the upper boundary) show both the highest values of Mode I and Mode II ERR  
 as well as the maximum increase with respect to the interactive case ( $1 \times 1 - free$   
 400 and  $1 \times 1 - coupling$ ). When the H-condition is applied to the upper bound-  
 ary, thus constraining the magnitude of the strain magnification effect, both the  
 magnitude of Mode I and Mode II ERR as well as their relative increase with  
 respect to the interactive case are significantly reduced.  $21 \times 1 - coupling + H$   
 represents, when considering both Mode I and Mode II ERR, the best approxi-  
 405 mation to the results of  $21 \times 1 - m \cdot t_{90^\circ}$ . The mechanisms at play are the same  
 as in Sec. 3.1: by keeping the  $0^\circ/90^\circ$  interface straight (coupling condition), the  
 $0^\circ$  layer favors an increase in  $G_I$  and decrease in  $G_{II}$  for small debonds and an  
 increase in  $G_{II}$  for large debonds; by applying a uniform  $x$ -strain on the  $90^\circ$   
 layer boundary (H-condition), the  $0^\circ$  layer promotes a more uniform  $x$ -strain in  
 410 the  $90^\circ$  layer and acts against the strain magnification effect, reducing debond  
 ERR. Results in Fig. 6 and Fig. 7 show that the latter effect (H-condition) is  
 dominant. It seems reasonable to conclude that debond growth is favored (i.e.  
 debond ERR is higher) in the presence of strain or stress concentrations (as for  
 example in the presence of a free surface or only coupling conditions on the ver-  
 415 tical displacement), while more uniform strain and stress fields as those created  
 by the proximity of the  $0^\circ/90^\circ$  interface reduce both Mode I and Mode II ERR  
 and thus tend to prevent debond growth.

### 3.3. *Effect of the presence of fiber rows with no damage on the debond- $0^\circ/90^\circ$ interface interaction*

420 After having investigated the effect of the proximity of the  $0^\circ/90^\circ$  interface  
 and of the thickness of the  $0^\circ$  layer on debond ERR for different cases of debond-  
 debond interaction in the same fiber row, we address in this section the effect  
 of the presence of fiber rows with only fully bonded fibers between debonds  
 and the  $0^\circ/90^\circ$  interface. In other words, we are separating the debond from

425 the  $0^\circ/90^\circ$  interface by inserting rows of fully bonded fibers in between. We  
 consider only the case  $m = 1$ , i.e.  $t_{0^\circ} = t_{90^\circ}$ , given that increasing the  $0^\circ$   
 layer thickness does not result in any remarkable effect on ERR as shown in  
 Sec. 3.1 and Sec. 3.2. Following the same philosophy of Sec. 3.1 and Sec. 3.2,  
 we analyze the effect of the presence of fiber rows with no damage on debond  
 430 ERR: first, when the central fiber row possesses only partially debonded fibers,  
 which represents the most severe damage state for these RUCs and the solution  
 for interactive debonds (models  $1 \times k - 1 \cdot t_{90^\circ}$  in Figures 8 and 9); second, the  
 case of debonds separated by  $n - 1$  fully bonded fibers in the central fiber row,  
 which corresponds to the least severe state of damage and to the solution for  
 435 non-interactive debonds (models  $21 \times k - 1 \cdot t_{90^\circ}$  in Figures 10 and 11).  
 Observation of Fig. 8, Fig. 9, Fig. 10 and Fig. 11 reveals that no difference can  
 be seen in Mode I and Mode II ERR by increasing the number  $k$  of rows with  
 undamaged fibers when  $k \geq 3$ , which means that debond ERR does not change  
 once at least 1 row of undamaged fibers is present between the debond and  
 440 the  $0^\circ/90^\circ$  interface. A significant change is visible only when  $k = 1$ , which  
 means that no row of undamaged fibers is present between the debond and the  
 $0^\circ/90^\circ$  interface. This change, from  $k \geq 3$  to  $k = 1$ , corresponds in particular  
 to a reduction of both  $G_I$  and  $G_{II}$ . The results of Figures 8, 9, 10 and 11  
 imply that the mechanisms of debond- $0^\circ/90^\circ$  interface interaction described in  
 445 Sec. 3.1 and Sec. 3.2 are actually very localized and that debond ERR is affected  
 by the presence of the  $0^\circ/90^\circ$  interface only when no fully bonded fiber is placed  
 in between. Given that the number  $k$  of fibers in the RUC vertical direction  
 corresponds to the thickness of the  $90^\circ$  ply measured in terms of number of  
 fiber rows present through its thickness, the results presented here point to  
 450 another conclusion: the ply-thickness effect does not seem to apply to debond  
 growth, unless an *ultra-thin* ply constituted by only one fiber row ( $k = 1$ )  
 is considered. Analogous results can be found in [36, 37], where the authors  
 investigate the ply-thickness effect on debond growth in cross-ply laminates  
 using: first, a single centrally-placed partially debonded fiber with surrounding  
 455 matrix corresponding to  $V_f = 55\%$ , embedded from all sides in a homogenized



90° ply bounded by homogenized 0° layers; second, one partially debonded fiber placed in the center and a second partially debonded fiber placed at an angle  $\theta_2$  with respect to the horizontal direction with surrounding matrix corresponding to  $V_f = 55\%$ , embedded from all sides in a homogenized 90° ply bounded by homogenized 0° layers. The thickness of the 0° layer is chosen as reference and a  $[0_p^\circ, 90_{r.p}^\circ]_S$  laminate is considered. Carbon-epoxy and glass-epoxy systems are both studied. The thickness of the 90° ply,  $t_{90^\circ} = r \cdot t_{0^\circ}$ , varies from  $r = 3$  (thick 90° ply,  $> 100$  fiber diameters) to  $r = 0.1$  (thin 90° ply,  $\sim 4 - 5$  fiber diameters). No measurable ply-thickness effect was observed. Experimental support to the claim that the ply-thickness effect has no influence on debond growth can be also found in the literature, in [6]. The authors conducted *in-situ* observations of edge micro-cracks with an optical microscope on  $[0_2^\circ, 90_n^\circ, 0_2^\circ]$  carbon fiber-epoxy laminates with  $n = 1, 2, 4$ , corresponding to a 90° ply thickness of respectively 40  $[\mu m]$  ( $\sim 6 - 8$  fiber diameters), 80  $[\mu m]$  ( $\sim 12 - 16$  fiber diameters) and 160  $[\mu m]$  ( $\sim 24 - 32$  fiber diameters). For  $n = 1$ , i.e. the case of a very thin 90° ply, isolated debonds appear at a lower value of the applied strain than in thicker plies (at 0.4% vs 0.7%) while growth and coalescence of debonds is suppressed and no transverse crack can be observed even at a strain of 1.5%. The ply-thickness effect was thus observed in [6] for transverse cracks, i.e. coalescence of debonds was delayed to higher strains and even suppressed, but not for debond growth. The analysis presented in this article brings new arguments to the claim that the ply-thickness effect does not influence the growth of debonds.

#### 4. Conclusions

Different models of Repeating Unit Cell, representing different cross-ply laminates, have been studied in order to investigate the effect of the presence of the 0° layer and of its thickness on debond Energy Release Rate for interactive and non-interactive debonds. A particular damage state is studied, in which only the central row of fibers of the 90° ply possesses debonds. The thickness of the 90° ply is measured in terms of the number of fiber rows in the layer; the

485  $0^\circ$  layer is on the other hand modelled as a homogenized material, the thick-  
ness of which is a multiple of the  $90^\circ$  ply thickness. In order to investigate  
the mechanisms of the debond- $0^\circ/90^\circ$  interface interaction, Mode I and Mode  
II ERR of cross-ply RUCs are compared with those of RUCs with equivalent  
boundary conditions on the upper boundary: free surface; coupling conditions  
490 on the vertical displacements; an applied linear distribution of the horizontal  
displacement; coupling conditions on the vertical displacements superimposed  
to an applied linear distribution of the horizontal displacement (this last com-  
bination represents the most extreme effect of the  $0^\circ$  layer on debond growth).  
It has been found that:

- 495 – by forcing the  $0^\circ/90^\circ$  interface to remain approximately straight and con-  
trolling the uniformity of the horizontal displacements in the composite  
(and thus in the  $90^\circ$  ply), the presence of the  $0^\circ$  layer causes more ho-  
mogeneous local (i.e. in the debond neighborhood) strains, reducing the  
ERR at the debond crack tip;
- 500 – when increasing the thickness of the  $0^\circ$  layer, the effect of the presence of  
the  $0^\circ$  layer on debond ERR remains the same as in the case  $t_{0^\circ} = t_{90^\circ}$ ;
- no effect of the  $90^\circ$  layer thickness, measured in terms of number of fiber  
rows, is observed; a reduction in ERR takes place only when the thickness  
is reduced to only one fiber row.

505 The results reported in this article strengthen the claim that the ply-thickness  
effect does not influence the growth of individual debonds, as previously sug-  
gested in the literature [6, 18, 36, 37].

## Acknowledgements

Luca Di Stasio gratefully acknowledges the support of the European School  
510 of Materials (EUSMAT) through the DocMASE Doctoral Programme and the  
European Commission through the Erasmus Mundus Programme.

## References

- [1] K. Kawabe, New spreading technology for carbon fiber tow and its application to composite materials, *Sen'i Gakkaishi* 64 (8) (2008) 262–267. doi:10.2115/fiber.64.p\_262.
- [2] K. Yamaguchi, H. Hahn, The improved ply cracking resistance of thin-ply laminates, in: *Proceedings of the 15<sup>th</sup> International Conference on Composite Materials (ICCM-15)*, SAMPE, 2005.
- [3] S. Sihn, R. Kim, K. Kawabe, S. Tsai, Experimental studies of thin-ply laminated composites, *Composites Science and Technology* 67 (6) (2007) 996–1008. doi:10.1016/j.compscitech.2006.06.008.
- [4] T. Yokozeki, Y. Aoki, T. Ogasawara, Experimental characterization of strength and damage resistance properties of thin-ply carbon fiber/toughened epoxy laminates, *Composite Structures* 82 (3) (2008) 382–389. doi:10.1016/j.compstruct.2007.01.015.
- [5] T. Yokozeki, A. Kuroda, A. Yoshimura, T. Ogasawara, T. Aoki, Damage characterization in thin-ply composite laminates under out-of-plane transverse loadings, *Composite Structures* 93 (1) (2010) 49–57. doi:10.1016/j.compstruct.2010.06.016.
- [6] H. Saito, H. Takeuchi, I. Kimpara, Experimental evaluation of the damage growth restraining in 90 layer of thin-ply cfrp cross-ply laminates, *Advanced Composite Materials* 21 (1) (2012) 57–66. doi:10.1163/156855112X629522.
- [7] A. Arteiro, G. Catalanotti, J. Xavier, P. Camanho, Notched response of non-crimp fabric thin-ply laminates, *Composites Science and Technology* 79 (2013) 97–114. doi:10.1016/j.compscitech.2013.02.001.
- [8] A. Arteiro, G. Catalanotti, J. Xavier, P. Camanho, Large damage capability of non-crimp fabric thin-ply laminates, *Composites Part A: Applied Science*

- and Manufacturing 63 (2014) 110–122. doi:10.1016/j.compositesa.2014.04.002.
- [9] R. Amacher, J. Cugnoni, J. Botsis, L. Sorensen, W. Smith, C. Dransfeld, Thin ply composites: Experimental characterization and modeling of size-effects, Composites Science and Technology 101 (2014) 121–132. doi:10.1016/j.compscitech.2014.06.027.
- [10] G. Guillaumet, A. Turon, J. Costa, J. Renart, P. Linde, J. Mayugo, Damage occurrence at edges of non-crimp-fabric thin-ply laminates under off-axis uniaxial loading, Composites Science and Technology 98 (2014) 44–50. doi:10.1016/j.compscitech.2014.04.014.
- [11] J. Cugnoni, R. Amacher, S. Kohler, J. Brunner, E. Kramer, C. Dransfeld, W. Smith, K. Scobbie, L. Sorensen, J. Botsis, Towards aerospace grade thin-ply composites: Effect of ply thickness, fibre, matrix and interlayer toughening on strength and damage tolerance, Composites Science and Technology 168 (2018) 467–477. doi:10.1016/j.compscitech.2018.08.037.
- [12] A. Kopp, S. Stappert, D. Mattsson, K. Olofsson, E. Marklund, G. Kurth, E. Mooij, E. Roorda, The aurora space launcher concept, CEAS Space Journal 10 (2) (2017) 167–187. doi:10.1007/s12567-017-0184-2.
- [13] J. E. Bailey, A. Parvizi, On fibre debonding effects and the mechanism of transverse-ply failure in cross-ply laminates of glass fibre/thermoset composites, Journal of Materials Science 16 (3) (1981) 649–659. doi:10.1007/bf02402782.
- [14] R. Krueger, K. N. Shivakumar, I. S. Raju, Fracture mechanics analyses for interface crack problems - a review, in: 54th AIAA/ASME/ASCE/AHS/ASC Structures, Structural Dynamics, and Materials Conference, American Institute of Aeronautics and Astronautics, 2013. doi:10.2514/6.2013-1476.

- [15] V. Kushch, S. Shmegeera, P. Brøndsted, L. Mishnaevsky, Numerical simulation of progressive debonding in fiber reinforced composite under transverse loading, *International Journal of Engineering Science* 49 (1) (2011) 17–29. doi:10.1016/j.ijengsci.2010.06.020.
- [16] L. P. Canal, C. González, J. Segurado, J. LLorca, Intraply fracture of fiber-reinforced composites: Microscopic mechanisms and modeling, *Composites Science and Technology* 72 (11) (2012) 1223–1232. doi:10.1016/j.compscitech.2012.04.008.
- [17] L. Bouhala, A. Makrady, S. Belouettar, H. Kiefer-Kamal, P. Frères, Modelling of failure in long fibres reinforced composites by x-FEM and cohesive zone model, *Composites Part B: Engineering* 55 (2013) 352–361. doi:10.1016/j.compositesb.2012.12.013.
- [18] M. Herráez, D. Mora, F. Naya, C. S. Lopes, C. González, J. LLorca, Transverse cracking of cross-ply laminates: A computational micromechanics perspective, *Composites Science and Technology* 110 (2015) 196–204. doi:10.1016/j.compscitech.2015.02.008.
- [19] V. Mantič, Interface crack onset at a circular cylindrical inclusion under a remote transverse tension. application of a coupled stress and energy criterion, *International Journal of Solids and Structures* 46 (6) (2009) 1287–1304. doi:10.1016/j.ijsolstr.2008.10.036.
- [20] Y. Freed, L. Banks-Sills, A new cohesive zone model for mixed mode interface fracture in bimaterials, *Engineering Fracture Mechanics* 75 (15) (2008) 4583–4593. doi:10.1016/j.engfracmech.2008.04.013.
- [21] Z.-H. Jin, C. Sun, Cohesive zone modeling of interface fracture in elastic bi-materials, *Engineering Fracture Mechanics* 72 (12) (2005) 1805–1817. doi:10.1016/j.engfracmech.2004.09.011.
- [22] L. E. Asp, L. A. Berglund, P. Gudmundson, Effects of a composite-like

- stress state on the fracture of epoxies, *Composites Science and Technology* 53 (1) (1995) 27–37. doi:10.1016/0266-3538(94)00075-1.
- [23] A. Pawlak, A. Galeski, A. Rozanski, Cavitation during deformation of semicrystalline polymers, *Progress in Polymer Science* 39 (5) (2014) 921–958. doi:10.1016/j.progpolymsci.2013.10.007.
- [24] R. Krueger, Virtual crack closure technique: History, approach, and applications, *Applied Mechanics Reviews* 57 (2) (2004) 109. doi:10.1115/1.1595677.
- [25] J. R. Rice, A path independent integral and the approximate analysis of strain concentration by notches and cracks, *Journal of Applied Mechanics* 35 (2) (1968) 379. doi:10.1115/1.3601206.
- [26] M. Toya, A crack along the interface of a circular inclusion embedded in an infinite solid, *Journal of the Mechanics and Physics of Solids* 22 (5) (1974) 325–348. doi:10.1016/0022-5096(74)90002-7.
- [27] F. París, J. C. Caño, J. Varna, The fiber-matrix interface crack — a numerical analysis using boundary elements, *International Journal of Fracture* 82 (1) (1996) 11–29. doi:10.1007/bf00017861.
- [28] L. Zhuang, A. Pupurs, J. Varna, R. Talreja, Z. Ayadi, Effects of inter-fiber spacing on fiber-matrix debond crack growth in unidirectional composites under transverse loading, *Composites Part A: Applied Science and Manufacturing* 109 (2018) 463–471. doi:10.1016/j.compositesa.2018.03.031.
- [29] M. Muñoz-Reja, L. Távara, V. Mantić, P. Cornetti, Crack onset and propagation at fibre–matrix elastic interfaces under biaxial loading using finite fracture mechanics, *Composites Part A: Applied Science and Manufacturing* 82 (2016) 267–278. doi:10.1016/j.compositesa.2015.09.023.
- [30] E. Correa, V. Mantić, F. París, Effect of thermal residual stresses on matrix failure under transverse tension at micromechanical level: A numerical and

experimental analysis, *Composites Science and Technology* 71 (5) (2011) 622–629. doi:10.1016/j.compscitech.2010.12.027.

- 625 [31] E. Correa, F. París, V. Mantič, Effect of the presence of a secondary transverse load on the inter-fibre failure under tension, *Engineering Fracture Mechanics* 103 (2013) 174–189. doi:10.1016/j.engfracmech.2013.02.026.
- [32] E. Correa, F. París, V. Mantič, Effect of a secondary transverse load on the inter-fibre failure under compression, *Composites Part B: Engineering* 65 (2014) 57–68. doi:10.1016/j.compositesb.2014.01.005.
- 630 [33] C. Sandino, E. Correa, F. París, Numerical analysis of the influence of a nearby fibre on the interface crack growth in composites under transverse tensile load, *Engineering Fracture Mechanics* 168 (2016) 58–75. doi:10.1016/j.engfracmech.2016.01.022.
- [34] C. Sandino, E. Correa, F. París, Interface crack growth under transverse compression: nearby fibre effect, in: *Proceeding of the 18<sup>th</sup> European Conference on Composite Materials (ECCM-18)*, 2018.
- 635 [35] J. Varna, L. Q. Zhuang, A. Pupurs, Z. Ayadi, Growth and interaction of debonds in local clusters of fibers in unidirectional composites during transverse loading, *Key Engineering Materials* 754 (2017) 63–66. doi:10.4028/www.scientific.net/kem.754.63.
- 640 [36] M. Velasco, E. Graciani, L. Távara, E. Correa, F. París, BEM multiscale modelling involving micromechanical damage in fibrous composites, *Engineering Analysis with Boundary Elements* 93 (2018) 1–9. doi:10.1016/j.enganabound.2018.03.012.
- 645 [37] F. París, M. L. Velasco, E. Correa, Micromechanical study on the influence of scale effect in the first stage of damage in composites, *Composites Science and Technology* 160 (2018) 1–8. doi:10.1016/j.compscitech.2018.03.004.

- [38] Simulia, Providence, RI, USA, ABAQUS/Standard User's Manual, Version  
650 6.12 (2012).
- [39] H. Zhang, M. Ericson, J. Varna, L. Berglund, Transverse single-fibre test  
for interfacial debonding in composites: 1. experimental observations, Com-  
posites Part A: Applied Science and Manufacturing 28 (4) (1997) 309–315.  
doi:10.1016/s1359-835x(96)00123-6.
- 655 [40] L. Di Stasio, J. Varna, Z. Ayadi, Energy release rate of the fiber/matrix  
interface crack in UD composites under transverse loading: effect of the  
fiber volume fraction and of the distance to the free surface and to non-  
adjacent debonds, Theoretical and Applied Fracture Mechanics (2019)  
102251doi:10.1016/j.tafmec.2019.102251.
- 660 [41] R. Teixeira, S. Pinho, P. Robinson, Thickness-dependence of the translam-  
inar fracture toughness: Experimental study using thin-ply composites,  
Composites Part A: Applied Science and Manufacturing 90 (2016) 33–44.  
doi:10.1016/j.compositesa.2016.05.031.
- [42] J. Garrido, A. Foces, F. Paris, B.e.m. applied to receding contact problems  
665 with friction, Mathematical and Computer Modelling 15 (3-5) (1991) 143–  
153. doi:10.1016/0895-7177(91)90060-k.
- [43] L. M. Keer, J. Dundurs, K. C. Tsai, Problems involving a receding contact  
between a layer and a half space, Journal of Applied Mechanics 39 (4)  
(1972) 1115. doi:10.1115/1.3422839.
- 670 [44] K. C. Tsai, J. Dundurs, L. M. Keer, Elastic layer pressed against a half  
space, Journal of Applied Mechanics 41 (3) (1974) 703. doi:10.1115/1.  
3423375.
- [45] Z. Hashin, Analysis of composite materials—a survey, Journal of Applied  
Mechanics 50 (3) (1983) 481. doi:10.1115/1.3167081.



- 675 [46] R. Christensen, K. Lo, Solutions for effective shear properties in three phase  
sphere and cylinder models, *Journal of the Mechanics and Physics of Solids*  
27 (4) (1979) 315–330. doi:10.1016/0022-5096(79)90032-2.
- [47] F. París, E. Correa, V. Mantič, Kinking of transversal interface cracks  
between fiber and matrix, *Journal of Applied Mechanics* 74 (4) (2007) 703.  
680 doi:10.1115/1.2711220.

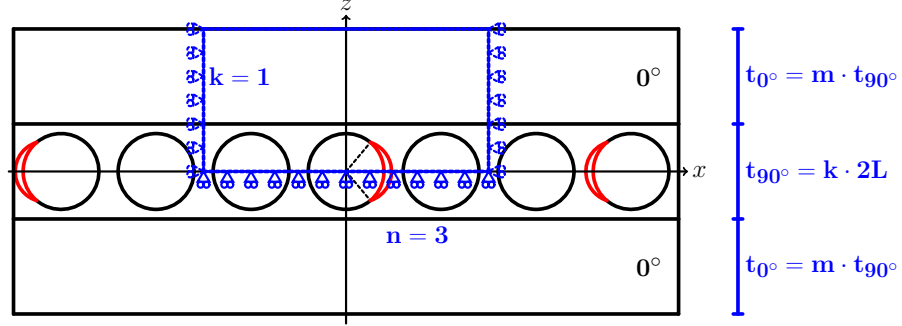


Figure 1: Models of  $[0_{m \cdot 1 \cdot 2L}^{\circ}, 90_{1 \cdot 2L}^{\circ}, 0_{m \cdot 1 \cdot 2L}^{\circ}]$  laminates with an ultra-thin  $90^{\circ}$  layer, where the  $90^{\circ}$  ply is made up by a single “row” of fibers. Debonds are repeating at different distances, measured in terms of the number  $n-1$  of fully bonded fibers appearing between two consecutive debonds.  $2L$  is the thickness of one-fiber row.

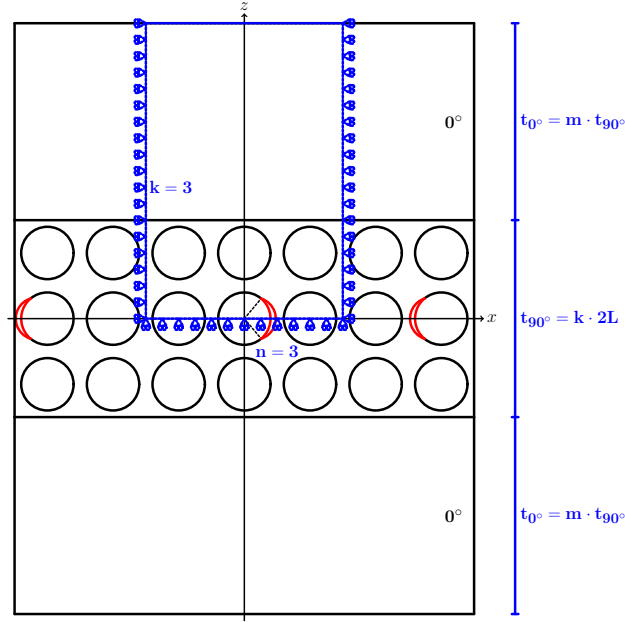


Figure 2: Models of  $[0_{m \cdot k \cdot 2L}^{\circ}, 90_{k \cdot 2L}^{\circ}, 0_{m \cdot k \cdot 2L}^{\circ}]$  laminates with a  $90^{\circ}$  layer of variable thickness, determined by the number  $k$  of “rows” of fibers along the vertical direction. Debonds are repeating at different distances along the horizontal direction, measured in terms of the number  $n-1$  of fully bonded fibers appearing between two consecutive debonds.  $2L$  is the thickness of one-fiber row.

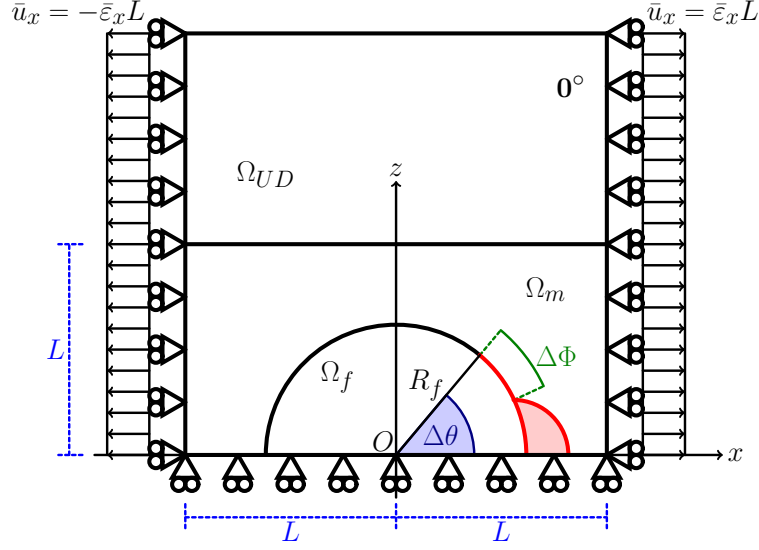


Figure 3: Schematic of the model with its main parameters.

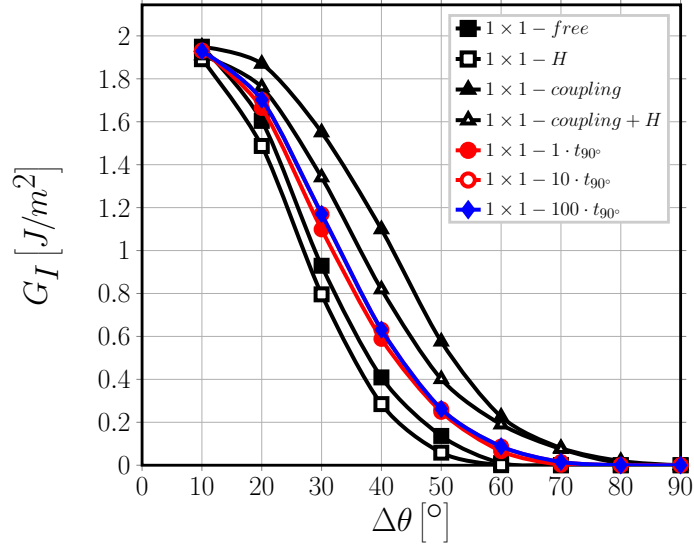


Figure 4: Effect of the proximity of the  $0^\circ/90^\circ$  interface and of the thickness of the  $0^\circ$  layer on Mode I ERR: models  $1 \times 1 - free$ ,  $1 \times 1 - H$ ,  $1 \times 1 - coupling$ ,  $1 \times 1 - coupling + H$  and  $1 \times 1 - m \cdot t_{90^\circ}$ .  $V_f = 60\%$ ,  $\bar{\varepsilon}_x = 1\%$ .

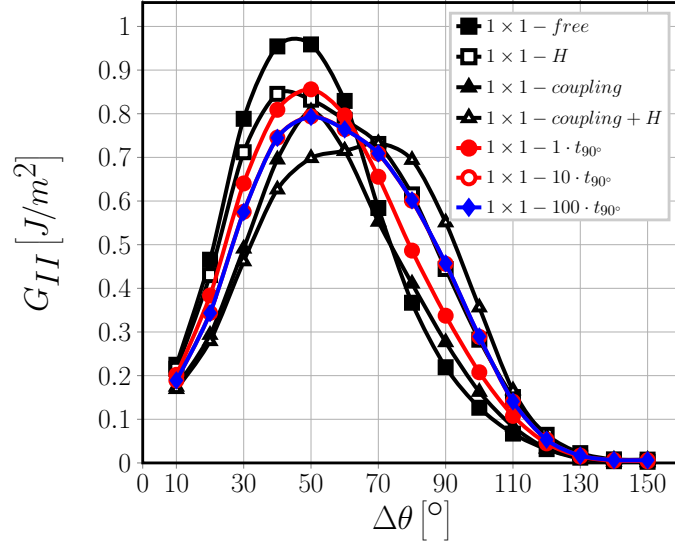


Figure 5: Effect of the proximity of the  $0^\circ/90^\circ$  interface and of the thickness of the  $0^\circ$  layer on Mode II ERR: models  $1 \times 1 - free$ ,  $1 \times 1 - H$ ,  $1 \times 1 - coupling$ ,  $1 \times 1 - coupling + H$  and  $1 \times 1 - m \cdot t_{90^\circ}$ .  $V_f = 60\%$ ,  $\bar{\varepsilon}_x = 1\%$ .

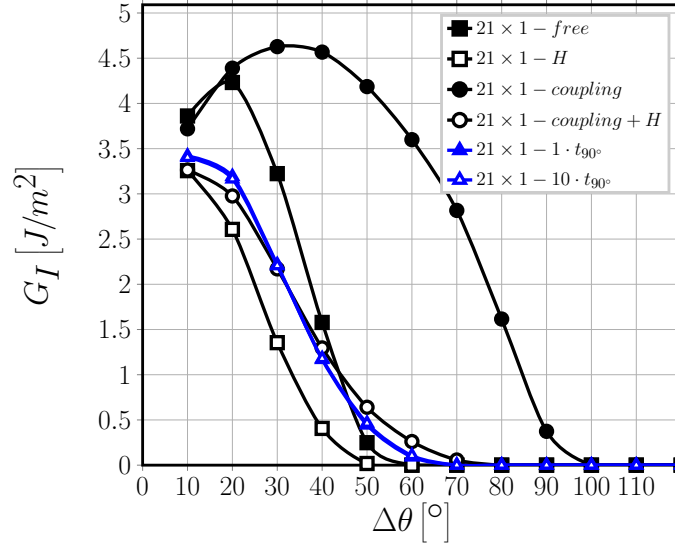


Figure 6: Effect of the presence of the  $0^\circ$  layer on Mode I ERR of non-interactive debonds: models  $21 \times 1 - free$ ,  $21 \times 1 - H$ ,  $21 \times 1 - coupling$ ,  $21 \times 1 - coupling + H$ ,  $21 \times 1 - 1 \cdot t_{90^\circ}$  and  $21 \times 1 - 10 \cdot t_{90^\circ}$ .  $V_f = 60\%$ ,  $\bar{\varepsilon}_x = 1\%$ .

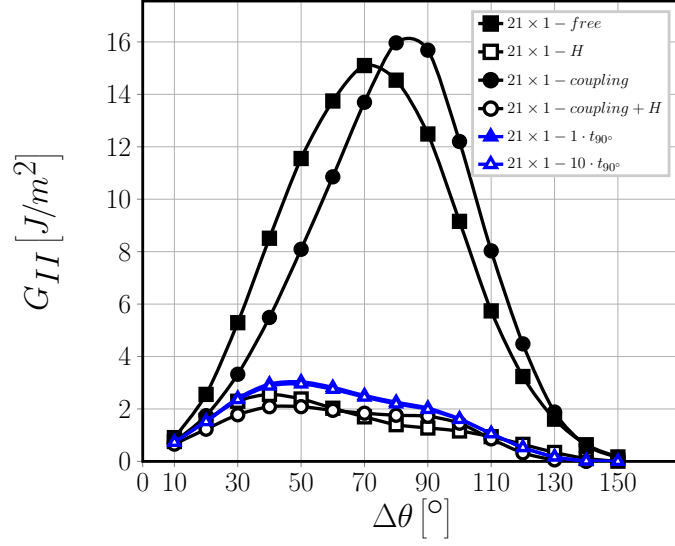


Figure 7: Effect of the presence of the  $0^\circ$  layer on Mode II ERR of non-interactive debonds: models  $21 \times 1 - free$ ,  $21 \times 1 - H$ ,  $21 \times 1 - coupling$ ,  $21 \times 1 - coupling + H$ ,  $21 \times 1 - 1 \cdot t_{90^\circ}$  and  $21 \times 1 - 10 \cdot t_{90^\circ}$ .  $V_f = 60\%$ ,  $\bar{\varepsilon}_x = 1\%$ .

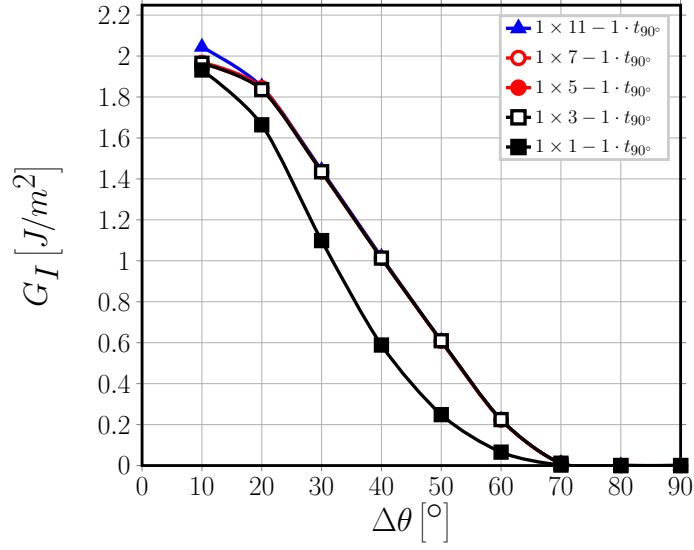


Figure 8: Effect of the presence of undamaged fiber rows in the  $90^\circ$  layer on debond- $0^\circ/90^\circ$  interface interaction for Mode I ERR: models  $1 \times k - 1 \cdot t_{90^\circ}$ .  $V_f = 60\%$ ,  $\bar{\varepsilon}_x = 1\%$ .

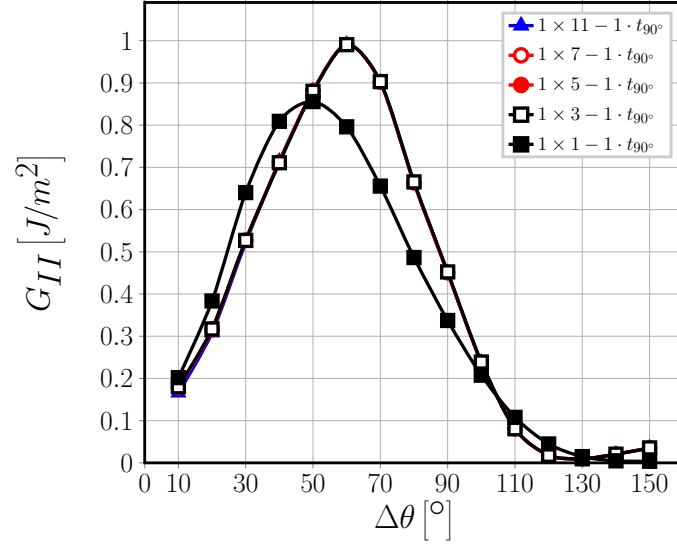


Figure 9: Effect of the presence of undamaged fiber rows in the  $90^\circ$  layer on debond- $0^\circ/90^\circ$  interface interaction for Mode II ERR: models  $1 \times k - 1 \cdot t_{90^\circ}$ .  $V_f = 60\%$ ,  $\bar{\varepsilon}_x = 1\%$ .

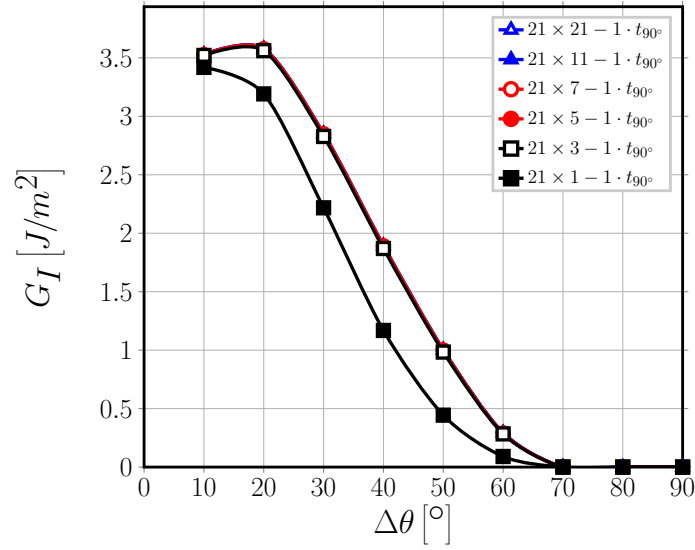


Figure 10: Effect of the presence of undamaged fiber rows in the  $90^\circ$  layer on debond- $0^\circ/90^\circ$  interface interaction for Mode I ERR: models  $n \times k - 1 \cdot t_{90^\circ}$ .  $V_f = 60\%$ ,  $\bar{\varepsilon}_x = 1\%$ .

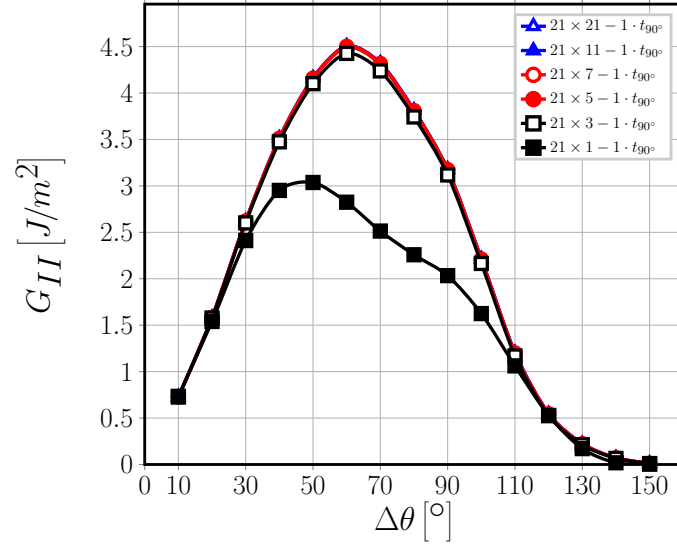


Figure 11: Effect of the presence of undamaged fiber rows in the  $90^\circ$  layer on debond- $0^\circ/90^\circ$  interface interaction for Mode II ERR: models  $n \times k - 1 \cdot t_{90^\circ}$ .  $V_f = 60\%$ ,  $\bar{\varepsilon}_x = 1\%$ .

Table 1: Summary of mechanical properties of fiber, matrix and UD layer.

Material	$V_f$ [%]	$E_L$ [GPa]	$E_T$ [GPa]	$G_{LT}$ [GPa]	$\nu_{LT}$ [-]	$\nu_{TT}$ [-]
Glass fiber	-	70.0	70.0	29.2	0.2	0.2
Epoxy	-	3.5	3.5	1.25	0.4	0.4
UD	60.0	43.442	13.714	4.315	0.273	0.465